Synthesis and characterization of magnetic mesoporous particles

Marco A. Morales [a], Artur J.S. Mascarenhas [b,c,*], Angelo M.S. Gomes [d], Carlos A.P. Leite [e], Heloysa M.C. Andrade [b,c], Caio M.C. de Castilho [a,c], Fernando Galembeck [e]

[a] Instituto de Física, Universidade Federal da Bahia (UFBA), Campus Universitário da Federação/Ondina, 40210-340 Salvador, BA, Brazil
[b] Instituto de Química, Universidade Federal da Bahia (UFBA), Campus Universitário da Federação/Ondina, 40170-280 Salvador, BA, Brazil
[c] Instituto Nacional de Ciência e Tecnologia de Energia e Ambiente, Universidade Federal da Bahia (UFBA), Campus Universitário da Federação/Ondina, 40170-280 Salvador, BA, Brazil
[d] Instituto de Física, Universidade Federal do Rio de Janeiro (UFRJ), Cidade Universitária, 21941-909 Rio de Janeiro, RJ, Brazil
[e] Instituto de Química, Universidade Estadual de Campinas (UNICAMP), Campus Universitário Zeferino Vaz, Caixa Postal 6154, 13083-862 Campinas, SP, Brazil

ARTICLE INFO

ABSTRACT

Magnetic mesoporous particles were synthesized and their magnetic and structural properties are reported. The synthesis procedure consists of four steps: (i) preparation of magnetite colloidal nanoparticles; (ii) growth of a silica layer; (iii) development of the mesoporous structure and (iv) template removal. Two different methods for the template removal were studied and their effectiveness was discussed. Magnetization and Mössbauer spectroscopy measurements showed superparamagnetic behavior for the particles at room temperature. X-ray diffraction and nitrogen adsorption measurements showed a mesoporous MCM-41 structure with 2.48 nm pore diameter and 1023 m^2/g total area.

© 2009 Elsevier Inc. All rights reserved.

1. Introduction

In the past several years there has been increasing interest in developing magnetic mesoporous particles, with enhanced textural properties that allow their use as adsorbents, catalysts or drug carriers. Some of the first results on this subject were performed by Kim et al. [1], who prepared mesoporous silica containing magnetite (Fe_3O_4) that was functionalized with amines and applied to Cu^{2+} removal from aqueous effluents. Since then, many papers have been published regarding the syntheses of magnetic mesoporous particles, containing iron oxides nuclei embedded in an ordered mesoporous SiO_2 matrix, as discussed below.

Iron oxides are mainly chosen due to their favorable magnetic properties, but also to their high availability, convenience of the preparation route and biocompatibility. Both magnetite and maghemite are ferrimagnetic, with magnetic transitions at about 800 K. Magnetite and maghemite have the highest saturation magnetizations among the iron oxides (90–95 emu/g and 60–80 emu/g, respectively) [2]. MCM-41 is the preferred mesoporous structure for the SiO_2 coating, as a result of its regular mesopores, whose diameters can be tailored between 1.5 and 10 nm using different

surfactants or co-surfactants in the synthesis process [3]. In addition, this material exhibits a very high surface area, high sorption capacity and good thermal stability [4,5].

Many synthesis methods have been investigated such as: (i) impregnation of iron precursors on previously synthesized mesoporous SiO_2 particles, followed by thermal and/or chemical treatment in order to produce magnetic nanoparticles, mainly magnetite or maghemite inside the porous structure [6–10]; (ii) coating of previously prepared Fe_3O_4 nanoparticles with mesoporous SiO_2, using a cationic or neutral surfactant as template [11–16]; (iii) reverse micro-emulsion techniques [17,18]; (iv) aerosol or spray-drying techniques [19–23]; (v) self-assembling [24,25]; (vi) phase transfer method [26], among others. Using one of these methods, or a combination of them, it has been possible to prepare particles with diameters ranging from nanometric to micrometric dimensions, with tailored morphological, magnetic and textural properties, according to the desired application. Specifically for drug magnetic targeting applications, it is desirable to produce nanosized particles, with high surface area and good responses to an external magnetic field gradient [27–30].

Recently, Deng et al. [31] have obtained superparamagnetic microspheres using a four-step procedure consisting of: (i) synthesis of Fe_3O_4 nanoparticles with a diameter of around 15 nm; (ii) development of a dense thin SiO_2 coating of ca. 20 nm; (iii) growing of a mesoporous SiO_2 shell whose mesopores are perpendicularly aligned towards the magnetite core and (iv) template

removal by acetone extraction. The final particles are microspheres whose diameters are of about 500 nm, with surface areas of 365 m^2/g and a saturation magnetization of 53.3 emu/g. This work reports the synthesis of magnetic mesoporous nanoparticles using a similar synthesis method, but producing particles with distinct morphological features and endowed with superior magnetic and textural properties. Two different routes for template removal were used and this step was found to have a decisive effect on particle properties.

2. Material and methods

2.1. Preparation of magnetic mesoporous particles

The samples were prepared in three steps: (i) preparation of colloidal iron oxide magnetic nanoparticles; (ii) coating of magnetic nanoparticles with a thick layer of SiO$_2$ and (iii) development of a mesoporous structure within the SiO$_2$ shell.

A magnetic colloidal solution was prepared by addition of tetraethylammonium hydroxide to the aqueous mixture of ferrous and ferric salts, according to Massart's method [32]. Briefly, 15 mL of a HCl solution (2 mol L^{-1}) was used to dissolve the iron salts. Then, 3 mL of iron(II) sulfate solution (2 mol L^{-1}) and 10 mL of an iron(III) chloride solution (1 mol L^{-1}) were mixed under vigorous mechanical stirring at room temperature. An aliquot of 50 mL of tetraethylammonium hydroxide (TEAOH) was added to the above solution until the solution reached a pH of 13. Immediately a black solution formed. After 20 min of stirring the particles were collected by centrifugation and washed three times. The particles were then redispersed in deionized water. Some sedimentation was observed after several minutes. The precipitate was thrown out and the black supernatant solution was kept. This suspension showed good dispersibility in deionized water.

The SiO$_2$ layer was grown on magnetic particles via the Stöber method [33]. It is known that silica-coated magnetic particles prepared in methanol produce a large number of very small silica particles without magnetic cores, due to methanol's relatively strong polarity as a solvent [34]. When ethanol is used during the silica-coating of magnetic particles, the particles have a relatively uniform dispersion and show typical core–shell structure with a relatively uniform size. Thus, by decreasing the alcohol polarity from methanol to propanol, the morphology of the obtained silica-coated magnetic particles becomes more irregular [34]. In this work, the ratio of ethanol to water used to prepare the sample was of 4/1. The sample was prepared by mixing 160 mL of ethanol, 40 mL of deionized water and 1 mL of ammonium hydroxide (25%) in a PTFE Teflon® beaker under magnetic stirring. An 8 mL aliquot of magnetic colloidal solution (c = 0.2 g L^{-1}) was added to the above solution. Then, 4 mL of TEOS was added slowly while stirring, at pH less than 10, to avoid fast polymerization of SiO$_2$.

The mesoporous structure was created using a method reported by Botella et al. [35] for the preparation of silver mesoporous core–shell particles. A solution was prepared with the following molar composition: SiO$_2$:0.11 CTABr:0.34 NaOH:395 H$_2$O:36 ethanol. This solution (pH 12.4) was then hydrothermally treated at 100 °C for 1.5 h in an autoclave. At the end of this process, the pH changed to 11. Particles were centrifuged at 9000 rpm for 0.5 h in an Eppendorf 5418 microcentrifuge (maximum of 1.68 × 10^4 g), and the solid material was taken, re-suspended in doubly distilled water, sonicated and centrifuged several times. The final powder was vacuum dried and kept in hermetically sealed centrifuge tubes. The template removal was studied by two different methods:

(i) Solvent extraction: the magnetic mesoporous particles were dispersed in the azeotropic mixture of ethanol/heptane at a

1:1 ratio and kept at 80 °C for 20 h. This procedure was repeated twice.

(ii) Calcination: the sample was calcined for 1 h at 300 °C under N$_2$ at a flow rate of 60 mL min^{-1}. To reach the desired temperature, the heating rate was set to 2 °C min^{-1}. This temperature was chosen in order to minimize agglomeration caused by sintering of the particles.

2.2. Characterization

Low and high angle X-ray diffraction (XRD) measurements were performed on a Shimadzu XRD6000 diffractometer operating with a Cu anode at 40 kV and 30 mA. Magnetic measurements were performed in a squid magnetometer from Quantum Design. The zero field cooled (ZFC) and field cooled (FC) measurements were performed at a field of 100 Oe. To image the particles, a Hitachi field emission scanning electron microscope was used. The particle size distribution was obtained from a Malvern dynamic light scattering (DLS) equipment. Thermogravimetric (TG) analyses were carried out in a Shimadzu TGA-50 instrument using a nitrogen flow. Fourier transformed infrared spectra (FTIR) were collected in a Perkin–Elmer Spectrum BX spectrometer. N$_2$ adsorption isotherms were determined at 77 K, after vacuum pretreating the samples at 323 K for 12 h in a Micromeritics ASAP2020 automated sorptometer. Mössbauer spectroscopy measurements were performed in transmission mode using a ^{57}Co:Rh source set in a sinusoidal mode. Mössbauer measurements were performed at room temperature and the spectra were analyzed using the software Normos 99. The reported isomer shift is relative to bcc iron at room temperature. Transmission electron microscopy (TEM) and electron-energy-loss spectroscopy (EELS) were done using a Carl Zeiss CEM-902 microscope equipped with a Castaing–Henry–Ottesmeyer energy filter within the column. Samples were prepared by placing a droplet of diluted particle dispersion on a parlodion-carbon coated microscope grid and drying under air.

3. Results and discussion

3.1. Iron oxide nanoparticles

The XRD pattern of the iron-oxide particles showed peaks that could be indexed either to magnetite (Fe$_3$O$_4$) or to maghemite (γ-Fe$_2$O$_3$). These iron oxides are ferrites with inverse spinel structure. Because of their structural similarities, these two iron oxides are difficult to distinguish by X-ray diffraction. The indexes used to label the XRD peaks in Fig. 1 are based on magnetite.

Additionally, the XRD pattern shows a non-flat background that seems to have a maximum at about 20° (2θ), which is very close to the peak (101) of poorly crystalline goethite (δ-FeOOH) [36]. The iron oxide nanoparticle diameter for the sample was 8.1 nm as obtained by an integral breadth analysis of the XRD peaks.

Magnetization versus field (M × H) measurements were performed at room temperature and at 2 K as shown in Fig. 2. The room temperature magnetization measurement showed a saturation magnetization of about 60 emu/g and a coercive field of 10 Oe. The low temperature measurement showed a hysteretic behavior with a coercive field of 280 Oe. These measurements demonstrated a flat behavior in the high field region. The low temperature saturation magnetization was of 76 emu/g.

The saturation magnetization for bulk magnetite ranges from 90–95 emu/g. The low saturation magnetization for this sample can be explained by considering that there might be a small fraction of a non-magnetic phase particles or that there might be canted surface spins [37]. As shown above in the XRD pattern, the broad peak could be related to a poorly crystalline goethite.
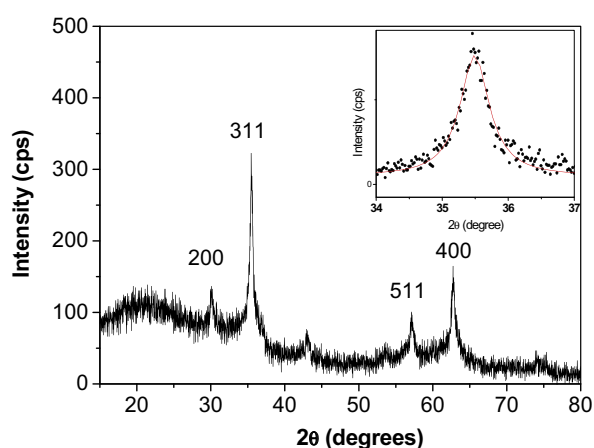
Fig. 1. X-ray powder diffraction of iron-oxide particles with peaks labels related to magnetite. The inset shows the fit to determine the particle size.
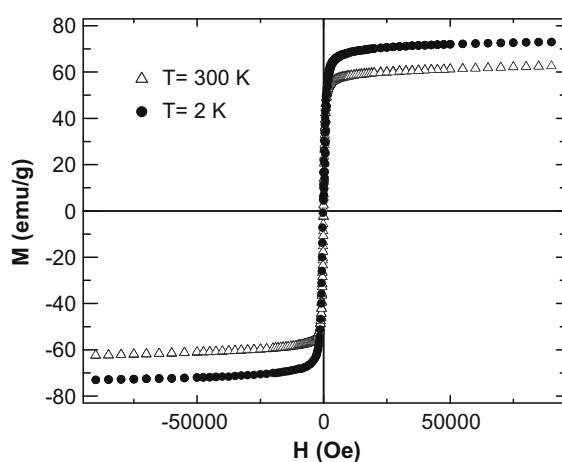

Fig. 2. $M \times H$ magnetization measurements for the iron-oxide nanoparticles at different temperatures.

Bulk goethite is an antiferromagnetic material with a Néel temperature of 410 K [36].

Mössbauer spectroscopy (MS) is a technique that provides important information about the state of the iron nuclei. Interpretation of the hyperfine parameters provides information about the

iron oxide phases and about their magnetic behavior. The MS measurement was performed at room temperature, and it showed a Zeeman-split spectrum with broad lines superposed on an unresolved background (Fig. 3).

The spectrum was fit to a distribution of magnetic hyperfine fields (Fig. 3b). The mean hyperfine magnetic field was approximately 47 T and the average isomer shift was 0.46 mm/s. There were no paramagnetic components. The unresolved background that appears in the distribution field for values smaller than 40 T could be related to the amorphous phase seen in the XRD measurements. Hyperfine field for bulk magnetite at room temperature ranges from 46 to 49 T, while for maghemite and goethite hyperfine fields are 50 and 35 T, respectively. The XRD, magnetization and Mössbauer spectroscopy measurements suggest that magnetite comprises a significant fraction of the sample.

3.2. Magnetic mesoporous particles

Although the Stöber method was developed to prepare spherical SiO_2 particles, in the current study this method was applied to deposit a SiO_2 layer on the magnetite particles. DLS (dynamic light scattering) measurements were performed to determine the particle size distribution, as shown in Fig. 4.

DLS is a useful technique for measuring the size of submicron particles. The intensity in scattering experiments depends on time, since the particles are in constant random motion. The intensity time dependence can be used to measure the diffusion coefficient of the particles and from this, the particle size can be determined. The intensity distribution is weighted according to the scattering intensity of each particle fraction, and the particle scattering intensity is proportional to the particle size. As such, the intensity distribution can be somewhat misleading, in that a small amount of aggregates or larger particles can dominate the distribution. In order to clarify this, both the intensity distribution (Fig. 4a) and the volume distribution (Fig. 4b) were plotted as a function of particle size. The volume distribution was provided by the Malvern equipment software.

Considering the volume distribution curve (Fig. 4a), it is clear that the small peak located at 75 nm is five times larger than the peak observed at the same position in the intensity distribution curve (Fig. 4b). Calculation of the relative contribution shows that the particles with main size of 220 nm represent 89% of the total particles. This result indicates that the scattering intensity mainly comes from the big particles.
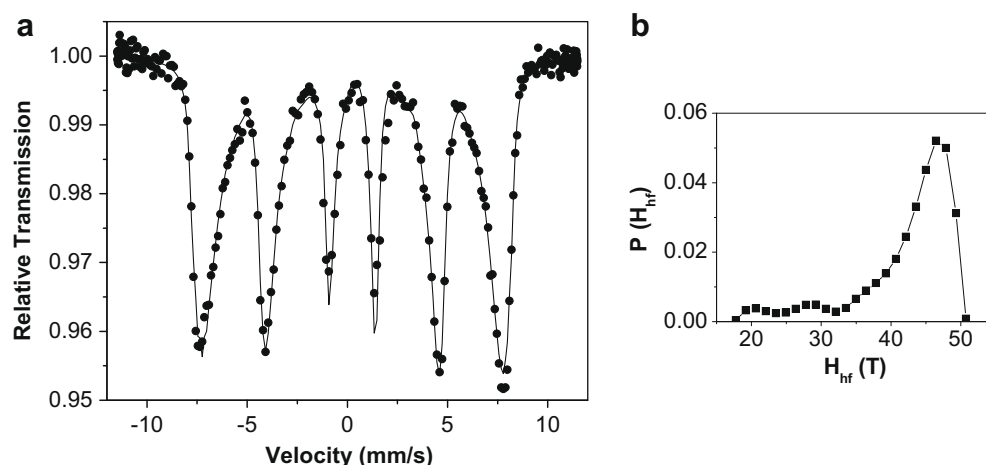

Fig. 3. Mössbauer spectroscopy measurements for the iron-oxide particles: (a) Mössbauer spectra and (b) distribution of magnetic hyperfine fields.
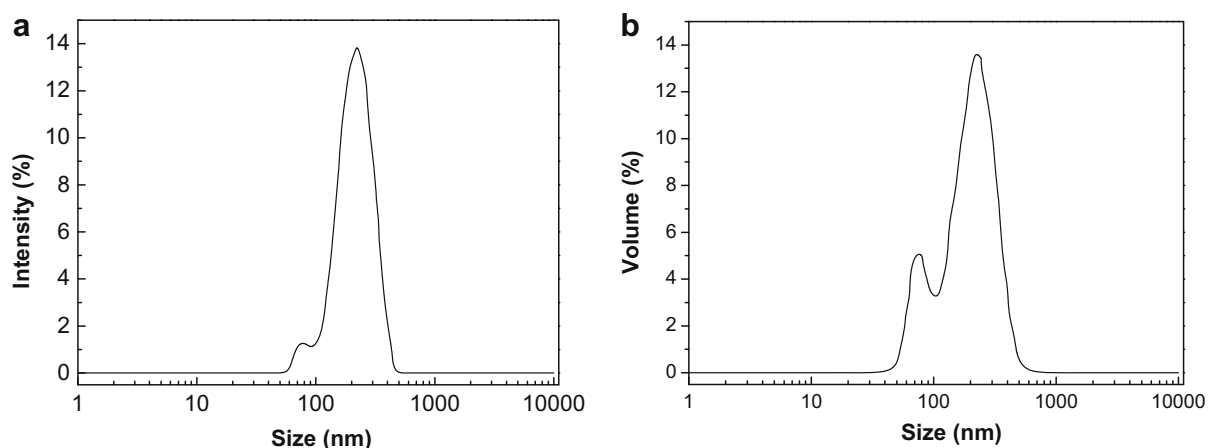
Fig. 4. Particle size distribution of the as-prepared magnetic mesoporous particles as determined by DLS: (a) intensity versus size; (b) volume fraction of particles versus size.

Transmission electron microscopy images of this sample showed the formation of aggregates (Fig. 5a). To further analyze the magnetic mesoporous particles, EELS was carried out. Fig. 5b shows L_{23} absorption peaks for Fe and Si in Fe_3O_4 and SiO_2, respectively. The Fe spectra exhibit two main lines labeled L_3 and L_2, which correspond to excitations from the spin–orbit split levels $2p_{3/2}$ and $2p_{1/2}$ followed by a steady plateau with very weak oscillations [38]. The Si spectra exhibit similar features as amorphous SiO_2 [39]. These measurements confirm the presence of the iron-oxide nanoparticles in the mesoporous particles.

The preparation of the mesoporous structure relies on the method used by Botella et al. [35]. CTABr micelles were used as templates to develop the porous structure. In the production of MCM-41 bulk materials, calcination at high temperature under air flow is the preferred method to remove the template, but, for nanoparticulated systems, this method has the disadvantage of producing aggregates. Thus, after developing the porous structure, the surfactant removal is a key step. To achieve this goal two methods were investigated. First, a solvent extraction method was attempted and, second, sample calcination under a N_2 flow was also tried.

In order to compare the efficiency of the template removal methods, TG/DTG experiments were carried out and the results are shown in Fig. 6.

For the as-prepared sample three regions of weight loss were observed: (i) from 25 to 125 °C, assigned to physisorbed water (3.03%); (ii) from 125 to 335 °C, due to the degradation of the organic template (CTA^+) interacting with silanol groups of the SiO_2 matrix (28.64%) and (iii) from 335 to 725 °C, attributed to thermal decomposition of carbonaceous residues (6.59%) and to silanol conversion to siloxane. This attribution is in accordance with previous data reported for MCM-41 bulk material [40].

For the solvent extracted sample, the same regions were observed and the weight losses were not significantly different from that for the as-prepared sample, corresponding to only 4.5%. Usually this method is used with a solution containing ethanol, heptane and HNO_3 or HCl [41], but removal of the surfactant with acidified ethanol could not be used in the present experiments because it would dissolve the iron-oxide nanoparticles. For the calcined particles, it was only observed a weight loss of 6.37% in the region "iii", indicating that some carbonaceous residues are still present.
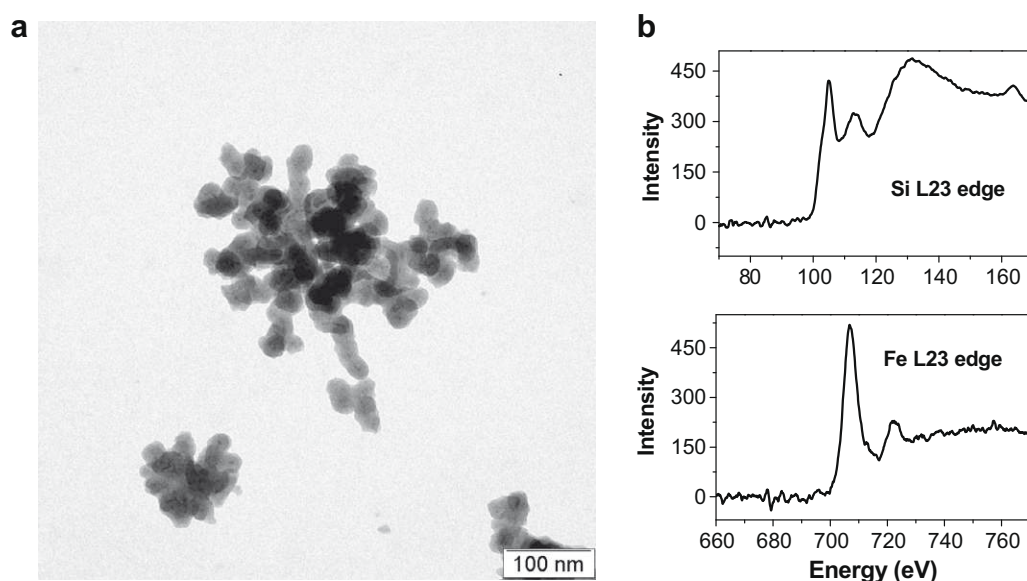

Fig. 5. (a) TEM image of the as-prepared magnetic mesoporous particles and (b) EELS spectra taken on the L_{23} edges for Fe and Si.
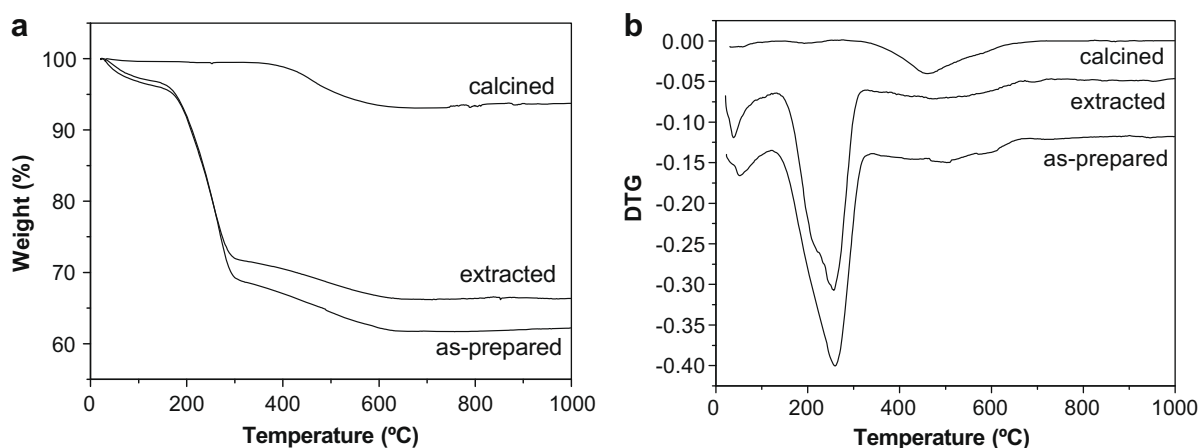
Fig. 6. Thermogravimetry (weight and differential signal, TG/DTG) profiles for the as-prepared, extracted and calcined samples.

These findings were further confirmed by FTIR spectroscopy, as can be seen in Fig. 7. Spectra baselines have been shifted in order to facilitate signals identification. The calcined sample FTIR spectra showed very low intensity peaks for the symmetric and asymmetric CH_2 stretching modes located at 2853 cm^{-1} and 2920 cm^{-1}, as well as for the CH_2 bending mode at 1475 cm^{-1}. These modes are related to the surfactant tail and their intensities are related to the surfactant concentration. Additionally, bands can be observed at *ca.* 3400 and 1650 cm^{-1} due to the stretching and bending of O–H bonds; at 1222 and 789 cm^{-1}, due to the external vibrations of SiO_4 chains; at 1066 and 720 cm^{-1} due to internal vibrations of SiO_4 units; at 962 cm^{-1}, due to asymmetric Si–O vibrations adjacent to sylanol groups; at 580 cm^{-1} due to the presence of double ring vibrations and 454 cm^{-1} due to the angular bending of Si–O units [42,43]. Magnetite usually presents bands at 570 and 375 cm^{-1}, due to Fe–O vibrations in tetrahedral and octahedral sites, respectively [44]. However, in the spectra of Fig. 7, such bands could not be observed because they are probably overlapped by the bands of SiO_2.

Even though the calcination temperature was mild, aggregation of the particles was observed. The DLS curve for the calcined sample showed a large peak at about 312 nm (Fig. 8).

Further evidence for the particle size enhancement was obtained by electron microscopy, in which images showed formation of aggregates of mesoporous particles (Fig. 9a). Small bright spots are discerned in the gray areas, with diameter in the 2–3 nm range (Fig. 9b), in agreement with the adsorption measurements.
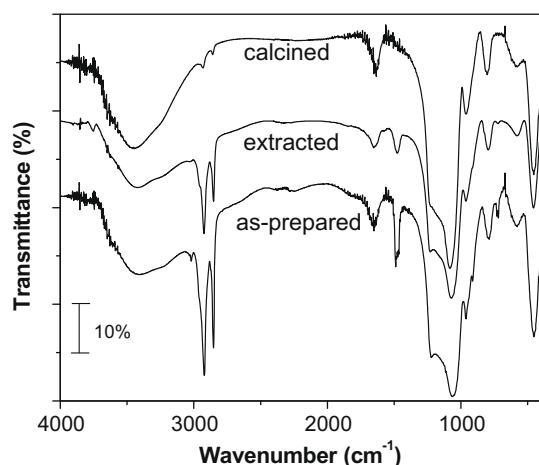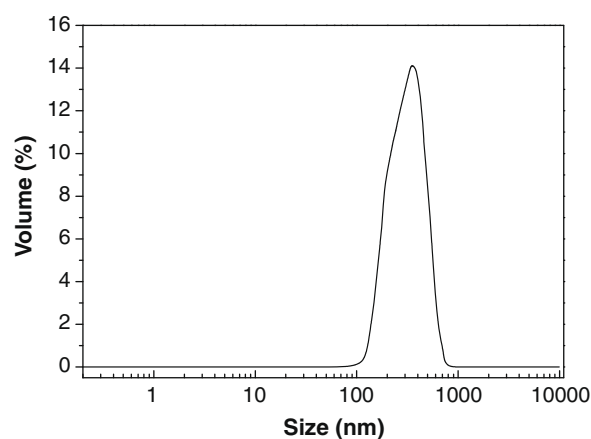

Fig. 8. Particle size distribution for the calcined magnetic mesoporous particles as determined by DLS.

Energy-filtered imaging in the transmission electron microscope, EFTEM, can be used in the low-energy-loss region to provide information on the distribution of chemical constituents within large particles and particle aggregates, as reported recently [45]. Inner morphological features which cannot be observed in bright-field mode are easily detected using low-energy-loss images from the same field. The elemental maps images were also obtained for Fe and Si using the iron L-edge and the silicon L-edge. The energy-selecting slits were set at 99 eV for Si-L_{23}, 708 eV for Fe-L_3 and 721 eV for Fe-L_2, using the three-windows method.

The bright-field image in Fig. 10 shows connected dark and gray domains. Bright areas in the Si map are dull in the Fe map and vice versa. The silicon map shows a bright matrix with many dark spots, while the iron map shows many bright spots within a dark matrix, indicating that iron oxide separate nanoparticles as well as aggregates are dispersed in the silica environment.

The low angle XRD pattern for the mesoporous particles consisted of two peaks. The first peak is located at 2.45° (d_{100} = 3.6 nm) and the second one is almost unresolved at 4.75° (d_{110} = 1.86 nm). These peaks are in agreement with the expected pattern for the MCM-41 material that usually shows a sharp peak between 2.1° (d_{100} = 4.21 nm) and 2.5° (d_{100} = 3.53 nm) [46]. Peak broadening is usually seen in structures with wormhole pore arrangements [47]. From the position of these peaks the cell lattice parameter was calculated to be approximately 4.7 nm. To enhance peak intensity in the XRD pattern, the intensity data were multiplied by 2θ and plotted against 2θ (inset in Fig. 11).

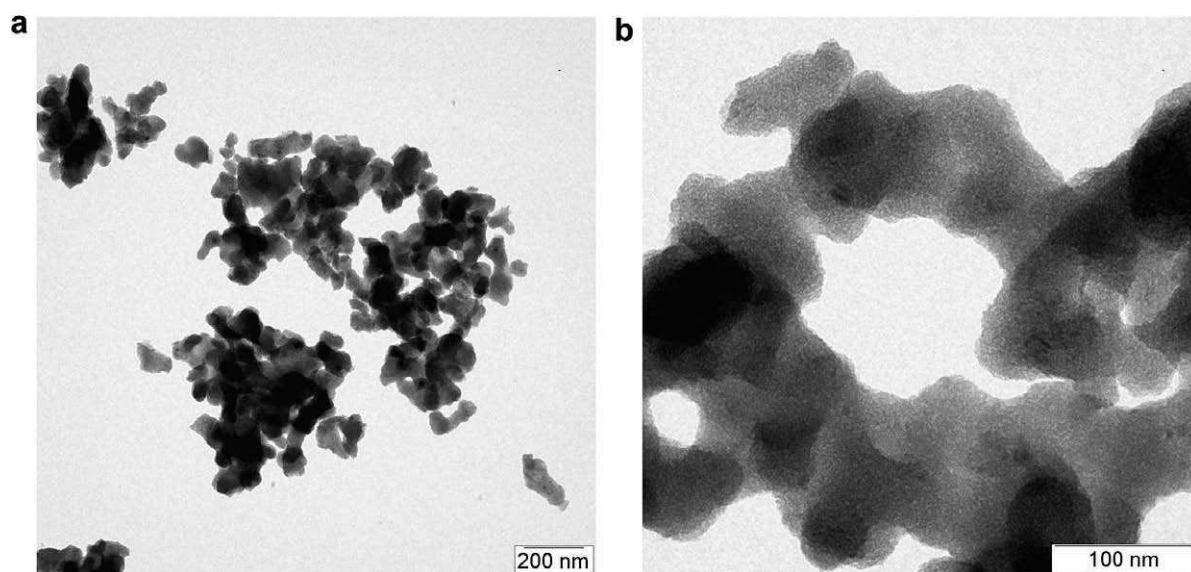**Fig. 7.** FTIR spectra for the as-prepared, extracted and calcined samples.

Fig. 9. TEM images of the calcined magnetic mesoporous particles showing: (a) larger aggregates formed after calcination and (b) porous nature of the silica matrix.
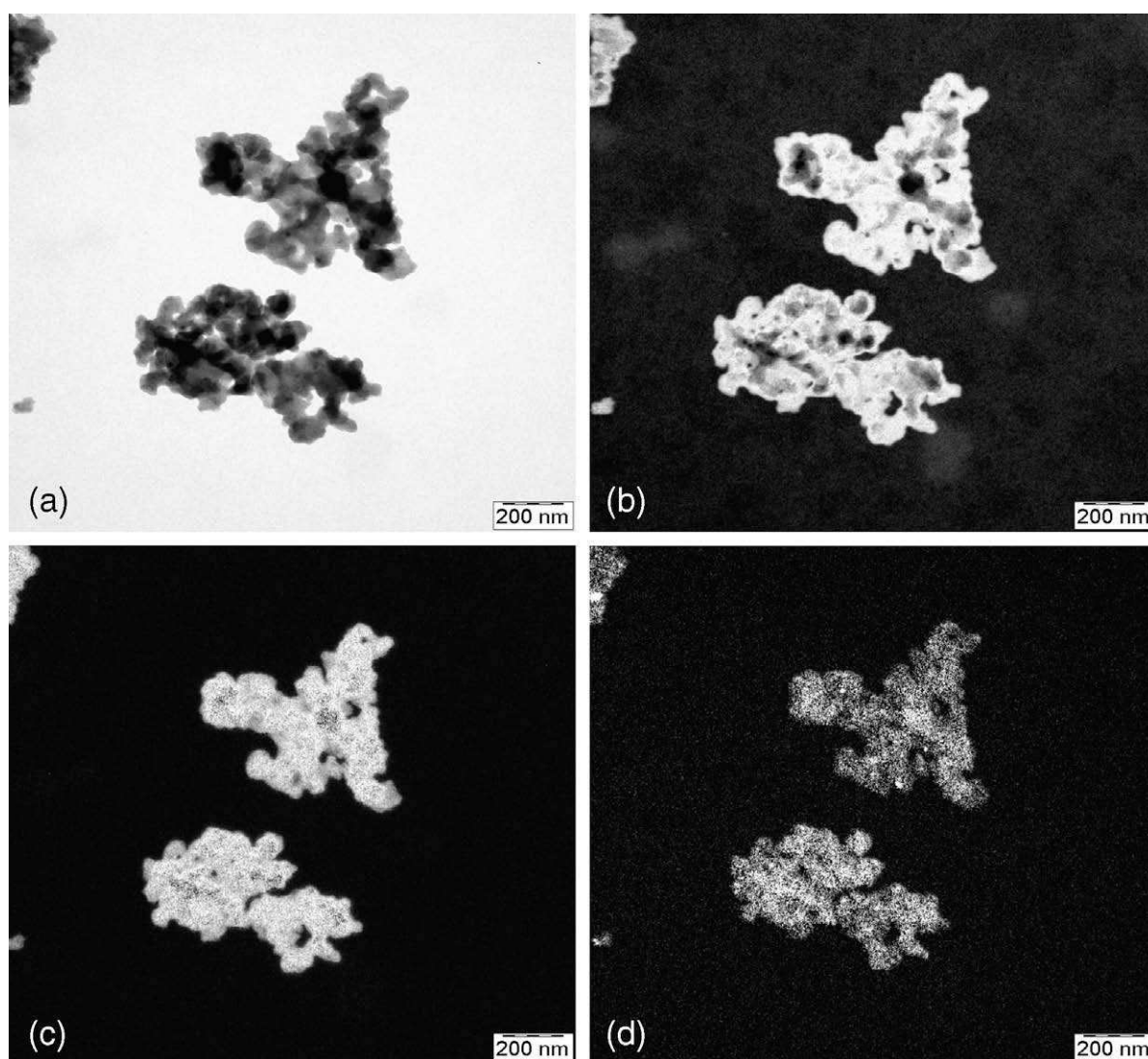

Fig. 10. (a) Bright-field image; (b) EFTEM (25 eV energy loss); (c) Si map and (d) Fe map for the calcined magnetic mesoporous particles.
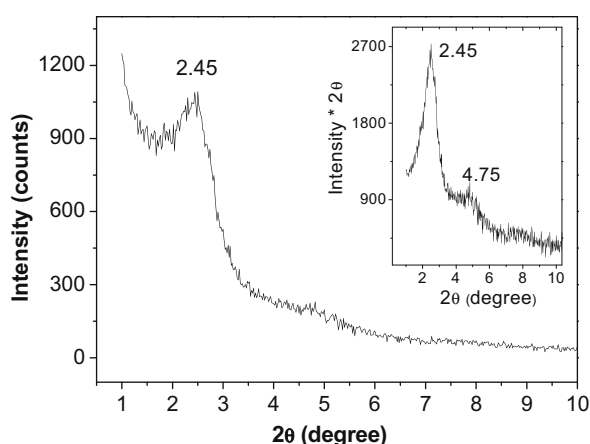
Fig. 11. XRD pattern of calcined mesoporous particles. The inset shows: (Intensity $\times 2\theta$) versus 2θ.

Examination of the samples by nitrogen sorption, Fig. 12, resulted in type IV isotherms (Fig. 12a) with pores of about 2.48 nm diameter (Fig. 12b), as determined by the Barrett–Joyner–Halenda (BJH) method. The high porosity indicated by the hysteresis at high relative pressures correlates to a specific surface area of approximately 1023 m^2/g. The large surface area and pore volumes determined by nitrogen sorption provide additional evidence for the successful removal of the template.
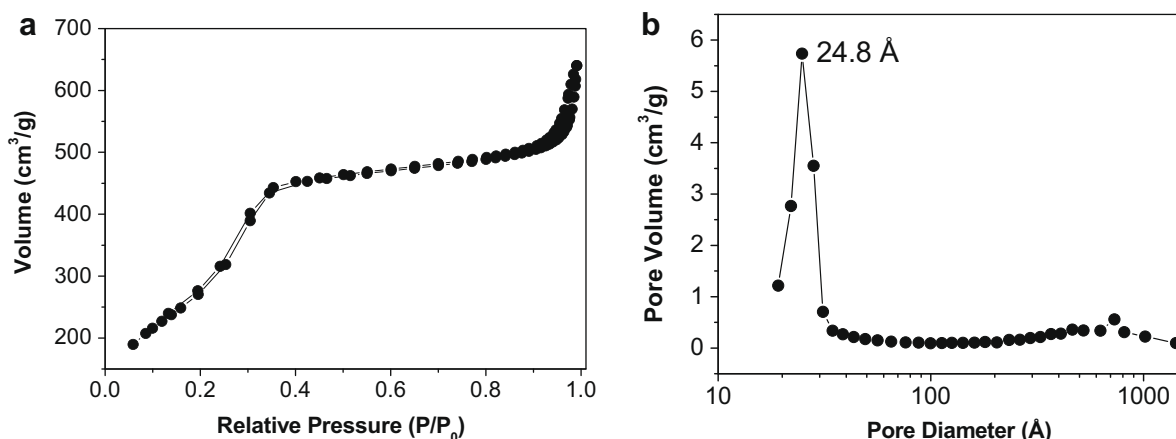
The magnetization versus temperature DC measurements for this sample showed a ZFC magnetization peak temperature at 95 K, and a ZFC and FC bifurcation temperature at about 200 K (Fig. 13). For a superparamagnetic system with a very narrow particle size distribution, the peak in the ZFC magnetization defines the blocking temperature and is normally very close to the bifurcation temperature between the ZFC and FC curves. In the present sample the bifurcation temperature is almost 100 K away from the ZFC peak temperature. This reflects the presence of a particle size distribution and interaction effects among the particles. In fact, the dipolar magnetic interaction can shift the blocking temperature to higher temperatures [48].

Magnetization versus field measurements at 5 K did not show magnetic saturation and the ferromagnetic loop showed a non-flat behavior even at fields as high as 5 T. The coercive field was 490 Oe and its magnetization at a field of 5 T was about 1.9 emu/g. At 300 K the loop showed a negligible coercive field and a negligible remanence. The higher coercive field might be related with magnetic pinning effects at the interface between the magnetite and the SiO_2 mesoporous structure. The surface spins would have such an effect on the core, avoiding the possibility of the core spins to rotate. Similar behavior was recently observed in maghemite nanoparticles embedded in a SiO_2 matrix [49].

The magnetization at high field showed a flat behavior and a magnetization at 5 T equal to 0.6 emu/g. This small value of the magnetization is due to normalization by the total mass. Similar values for the high field magnetization in the 300 K $M \times H$

Fig. 12. (a) Nitrogen adsorption and desorption isotherms and (b) pore size distribution for the calcined magnetic mesoporous particles.
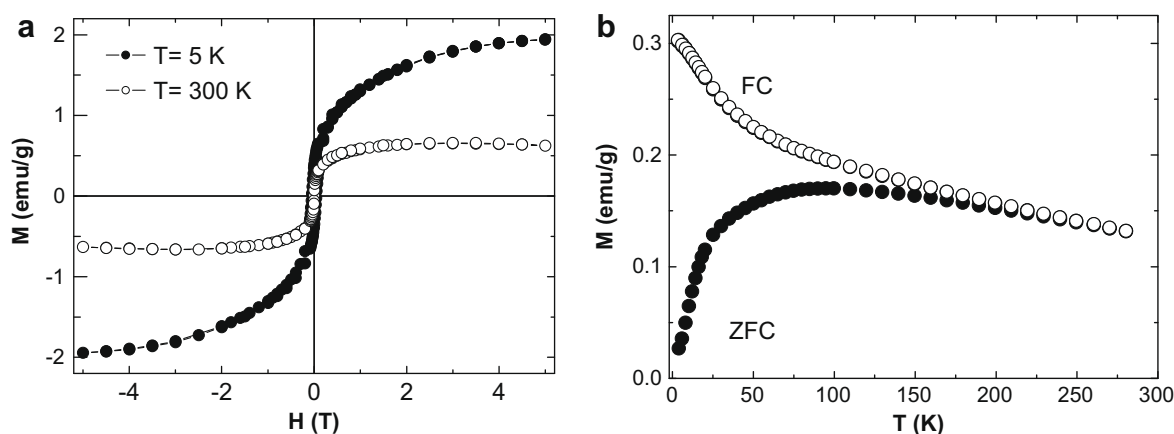

Fig. 13. Magnetization measurements for the calcined magnetic mesoporous particles at different temperatures: (a) magnetization versus H field; (b) magnetization versus temperature.
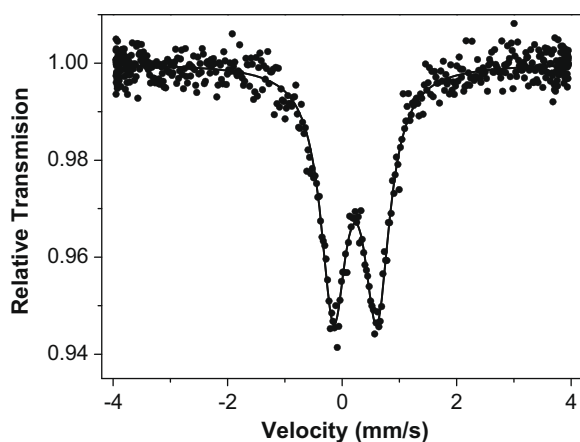
Fig. 14. Mössbauer spectroscopy measurements performed at room temperature for calcined magnetic mesoporous particles.

measurement were reported for SiO_2 coated magnetite particles. However, in that case the particles were not submitted to any thermal treatment [50].

Although the iron-oxide particles reported here have a mean diameter of 8.1 nm, their magnetic relaxation time would be different based on the size distribution, morphology and interaction effects. The critical size for a single magnetic domain depends on several factors, including particle size and shape. For most magnetic particles, estimates of the single domain to multi domain transition size are based on theoretical calculations. For magnetite (assuming a particle spherical shape) the best estimate for the transition size is about 80 nm [51]. Also, it was reported that the maximum critical diameter for a single domain particle of magnetite and maghemite is in the range of 30–100 nm [52].

The Mössbauer spectrum recorded at room temperature (Fig. 14) shows only a paramagnetic component caused by magnetically unblocked particles.

The phenomenon of superparamagnetism in Mössbauer spectroscopy originates from the thermal fluctuations of fine particles that cause the direction of the associated magnetic moments to vary with a relaxation frequency that depends upon the particle size, anisotropy energy and temperature. If the relaxation frequency is greater than the Larmor frequency of the ^{57}Fe probe (approximately 108 s^{-1}) the magnetic hyperfine splitting collapses and turns into a paramagnetic sub-spectrum. Around the Mössbauer blocking temperature, the relaxation frequency approaches the nuclear Larmor frequency and the spectrum should be composed of two sub-spectra, including a broad sextet related to the blocked particles and a paramagnetic sub-spectrum related to the unblocked particles (each one having a relative absorption area of around 50%). This result is in agreement with the $M \times T$ measurements.

4. Summary

Magnetic mesoporous particles with unprecedented but desirable properties were synthesized by a simple four-step procedure. Solvent extraction was not efficient for template removal and calcination showed to be a better route, despite causing some nanoparticle aggregation. Composite particle size is about 300 nm and total surface area is 1023 m^2/g showing superparamagnetic behavior at room temperature. This composite offers many possibilities to tailor the material for a wide range of applications including hydrophilic and hydrophobic drug carrying therapies via magnetic targeting as well as selective drug extraction from complex biolog-

ical environments, offering a combination of high load with narrow pore size distribution.

References

[1] Y. Kim, B. Lee, J. Yi, Sep. Sci. Technol. 38 (2003) 2533.
[2] B.D. Cullity, C.D. Graham, Introduction to Magnetic Materials, J. Wiley & Sons, New York, 2008.
[3] J.S. Beck, J.C. Vartuli, W.J. Roth, M.E. Leonowicz, C.T. Kresge, K.D. Schmitt, C.T.W. Chu, D.H. Olson, E.W. Sheppard, S.B. McCullen, J.B. Higgins, J.L. Schlenker, J. Am. Chem. Soc. 114 (1992) 10834.
[4] V.B. Fenelonov, V.N. Romannikov, A.Y. Derevyankin, Microporous Mesoporous Mater. 28 (1999) 57.
[5] G. Gu, P.P. Ong, C. Chu, J. Phys. Chem. Solids 60 (1999) 943.
[6] H.J. Kim, J.-E. Ahn, S. Haam, Y.-G. Shul, S.-Y. Song, T. Tatsumi, J. Mater. Chem. 16 (2006) 1617.
[7] T. Nakamura, Y. Yamada, K. Yano, J. Mater. Chem. 16 (2006) 2417.
[8] P. Wang, Y. Zhu, X. Yang, C. Li, Colloids Surf. A 294 (2007) 287.
[9] R.S. Prakasham, G.S. Devi, K.R. Laxmi, Ch.S. Rao, J. Phys. Chem. C 111 (2007) 3842.
[10] H.H.P. Yiu, S.C. McBain, A.J. ElHaj, J. Dobson, Nanotechnology 43 (2007) 435601.
[11] W. Zhao, J. Gu, L. Zhang, H. Chen, J. Shi, J. Am. Chem. Soc. 127 (2005) 8916.
[12] T. Sem, A. Sebastianelli, I.J. Bruce, J. Am. Chem. Soc. 128 (2006) 7130.
[13] M. Arruebo, W.Y. Ho, K.F. Lam, X. Chen, J. Arbiol, J. Santamaría, K.L. Yeung, Chem. Mater. 20 (2008) 486.
[14] K.C. Souza, G. Salazar-Alvarez, J.D. Ardisson, W.A.A. Macedo, E.M.B. Sousa, Nanotechnology 19 (2008) 185603.
[15] M. Liong, J. Lu, M. Kovochich, T. Xia, S.G. Ruehm, A.E. Nel, F. Tamanoi, J.I. Zink, ACS Nano 2 (2008) 889.
[16] S. Guo, D. Li, L. Zhang, J. Li, E. Wang, Biomaterials 30 (2009) 1881.
[17] D.K. Yi, S.S. Lee, G.C. Papaefthymiou, J.Y. Ying, Chem. Mater. 18 (2006) 614.
[18] J. Yu, H. Zhao, L. He, H. Yang, S. Ku, N. Yang, N. Xiao, J. Mater. Chem. 19 (2009) 1265.
[19] B. Julián-López, C. Boissière, C. Chanéac, D. Grosso, S. Vasseur, S. Miraux, E. Duguet, C. Sanchez, J. Mater. Chem. 17 (2007) 1563.
[20] T. Zheng, J. Pang, G. Tan, J. He, G.L. McPherson, Y. Lu, V.T. John, J. Zhan, Langmuir 23 (2007) 5143.
[21] E. Ruiz-Hernández, A. López-Noriega, D. Arcos, I. Isquierdo-Barba, O. Terasaki, M. Vallet-Regí, Chem. Mater. 19 (2007) 3455.
[22] E. Ruiz-Hernández, A. López-Noriega, D. Arcos, M. Vallet-Regí, Solid State Sci. 10 (2008) 421.
[23] L. Guo, J. Li, L. Zhang, J. Li, Y. Li, C. Yu, J. Shi, M. Ruan, J. Feng, J. Mater. Sci. 18 (2008) 2733.
[24] S. Zhu, Z. Zhou, D. Zhang, C. Jin, Z. Li, Microporous Mesoporous Mater. 106 (2007) 56.
[25] L. Qu, S. Tie, Microporous Mesoporous Mater. 117 (2009) 402.
[26] M. Asada, Y. Hara, Y. Kuroda, S. Tanaka, T. Horikawa, Y. Miyake, Ind. Eng. Chem. Res. 19 (2009) 1265.
[27] F. Torney, B.G. Trewyn, V.S.Y. Lin, K. Wang, Nat. Nanotechnol. 2 (2007) 295.
[28] C.Y. Lai, J. Am. Chem. Soc. 125 (2003) 4451.
[29] T.K. Jain, M.A. Morales, S.K. Sahoo, D.L. Leslie-Pelecky, V. Labhasetwar, Mol. Pharm. 2 (2005) 194.
[30] C. Alexiou, A. Schmidt, R. Klein, P. Hulin, C. Bergemann, W. Arnold, J. Magn. Magn. Mater. 252 (2002) 363.
[31] Y. Deng, D. Qi, C. Deng, X. Zhang, D. Zhao, J. Am. Chem. Soc. 130 (2008) 28.
[32] R. Massart, IEEE Trans. Magn. 17 (1981) 1247.
[33] A. Philipse, M.P.B. Bruggen, C. Pathmamanoharam, Langmuir 10 (1994) 92.
[34] H. Wang, H. Nakamura, Chem. Lett. 11 (2001) 1168.
[35] P. Botella, A. Corma, M. Navarro, Chem. Mater. 19 (2007) 1979.
[36] R.M. Cornell, U. Schwertmann, The Iron Oxides, Wiley VCH Verlag, Weinheim, Germany, 2003.
[37] J.M.D. Coey, Phys. Rev. Lett. 27 (1971) 1140.
[38] C. Colliex, T. Manoubi, C. Ortiz, Phys. Rev. B 44 (1991) 11402.
[39] <http://people.ccmr.cornell.edu/~davidm/WEELS/View/Si_oxy_SiO2.html> (accessed 25.09.08).
[40] W.A. Gomes Jr., L.A.M. Cardoso, A.R.E. Gonzaga, L.G. Aguiar, H.M.C. Andrade, Mater. Chem. Phys. 93 (2005) 133.
[41] K. Moller, T. Bein, R.X. Fischer, Chem. Mater. 11 (1999) 665.
[42] W. Que, Y. Zhou, Y.L. Lam, Y.C. Chan, C.H. Kam, Thin Solid Films 358 (2000) 16.
[43] A.V. Rao, R.R. Kalesh, G.M. Pajonk, J. Mater. Sci. 38 (2003) 4407.
[44] A. Pradeep, G. Chandrasekaran, Mater. Lett. 60 (2006) 371.
[45] L.F. Valadares, F.C. Bragança, C.A. Silva, C.A.P. Leite, F.J. Galembeck, J. Colloid Interface Sci. 309 (2007) 140.

[46] J. Rathousky, M. Zukalova, P.J. Kooyman, A. Zukal, Colloids Surf. A 241 (2004) 81.
[47] Q. Cai, W.-Y. Lin, F.-S. Xiao, W.-Q. Pang, X.-H. Chen, B.-S. Zou, Microporous Mesoporous Mater. 32 (1999) 1.
[48] C. Binns, M.J. Maher, Q.A. Pankhurst, D. Kechrakos, K.N. Trohidou, Phys. Rev. B 66 (2002) 184413.
[49] D. Ortega, J.S. Garitaonandía, C. Barrera-Solano, M. Domínguez, Sens. Actuators A 142 (2008) 554.
[50] Y.H. Deng, C.C. Wang, J.H. Hu, W.L. Yang, S.K. Fu, Colloids Surf. A 262 (2005) 87.
[51] R.F. Butler, J. Banerjee, Geophys. Res. 80 (1975) 4049.
[52] H. Soffel, Palaeomagnetismus and Archaeomagnetismus, Springer, Berlin, 1991.